Nucleation of Dislocations in 3.9 nm Nanocrystals at High Pressure

Abhinav Parakh, Sangryun Lee, K. Anika Harkins, Mehrdad T. Kiani, David Doan, Martin Kunz, Andrew Doran, Lindsey A. Hanson, Seunghwa Ryu, and X. Wendy Gu

1   **Nucleation of Dislocations in 3.9 nm Nanocrystals at High Pressure**

2   **Authors:** Abhinav Parakh[1], Sangryun Lee[2], K. Anika Harkins[3], Mehrdad T. Kiani[1], David

3   Doan[4], Martin Kunz[5], Andrew Doran[5], Lindsey A. Hanson[3], Seunghwa Ryu[2] and X. Wendy

4   Gu[4]*

5   **Affiliations:**

6   [1]Materials Science and Engineering, Stanford University, Stanford, CA 94305, USA.

7   [2]Mechanical Engineering, KAIST, Yuseong-gu, Daejeon 34141, Republic of Korea.

8   [3] Chemistry, Trinity College, Hartford, CT 06106, USA.

9   [4]Mechanical Engineering, Stanford University, Stanford, CA 94305, USA.

10   [5]Advanced Light Source, Lawrence Berkeley National Lab, Berkeley 94720, USA.

11

12   *Corresponding author:

13   X. Wendy Gu

14   452 Escondido Mall, Room 227, Stanford University, Stanford, CA 94305

15   650-497-3189

16   xwgu@stanford.edu

17

18   **Abstract:**

19   As circuitry approaches single nanometer length scales, it has become important to predict the

20   stability of single nanometer-sized metals. The behavior of metals at larger scales can be

21   predicted based on the behavior of dislocations, but it is unclear if dislocations can form and be

22   sustained at single nanometer dimensions. Here, we report the formation of dislocations within

23   individual 3.9 nm Au nanocrystals under nonhydrostatic pressure in a diamond anvil cell. We

24   used a combination of x-ray diffraction, optical absorbance spectroscopy, and molecular

25   dynamics simulation to characterize the defects that are formed, which were found to be surface-

26   nucleated partial dislocations. These results indicate that dislocations are still active at single

27   nanometer length scales and can lead to permanent plasticity.

28

29   **Main text:**

30   Permanent plastic deformation occurs in bulk crystalline metals that are subjected to large strains

31   at room temperature. This irreversible deformation can be due to the short-range interactions

32   between dislocations, or the formation of dislocation arrays at grain or twin boundaries.

33   Recently, reversible deformation from large strains has been observed in sub-10 nm Ag

34   nanocrystals [1] and 3.9 nm Au nanocrystals, [2] in which the nanocrystal rapidly recovers from

35   a flattened state after load is removed, and reverts to its original faceted shape. The mechanisms

36   behind this behavior remain unclear, as there is evidence for both diffusion and dislocation

37   mediated plasticity. Rapid diffusion of atoms at free surfaces and stress-induced diffusion at the

38   nanocrystal-indenter and nanocrystal-substrate interfaces have been proposed as mechanisms,

39   based on theoretical considerations and *in situ* transmission electron microscope (TEM)

40   observations [1,3]. Others have instead observed surface-nucleated dislocations and deformation

41   twinning in sub-10 nm nanowires, and stacking faults tetrahedra in sub-20 nm nanowires under

42   tension in both experiments and molecular dynamics (MD) simulations [4–7]. Dislocations and

43   diffusion may also act cooperatively. *In situ* TEM tension tests on ~20 nm and sub 5 nm Ag

44   nanowires showed that surface diffusion is enhanced at surface steps created by the passage of

45   dislocations [8,9]. Previous work from our group showed that pseudoelastic shape recovery

46 (diffusion mediated process) in 3.9 nm Au nanocrystals is accompanied by the formation of

47 irreversible defects, but the nature of the defects could not be determined [2].

48   These observations prompt the questions: Is there a limit to plasticity at small length

49 scales? What is the smallest crystal in which dislocations can form and lead to irreversible

50 deformation? This is critical to the processing and mechanical behavior of nanostructured

51 materials such as nanocrystalline, nanotwinned and nanoporous metals, and the design of stable

52 nano-devices with single nanometer metallic features [10]. To answer these questions,

53 deformation mechanisms in very small nanocrystals must be experimentally determined, but this

54 remains challenging. *In situ* TEM mechanical testing is the leading method to investigate

55 deformation mechanisms at this length scale, but results may be influenced by heating from the

56 electron beam. In addition, fast dislocations and dislocations that are invisible at specific imaging

57 conditions cannot be observed. X-ray diffraction (XRD) is another method to measure elastic

58 strain and defect formation in metals under mechanical stress. The width and relative intensities

59 of XRD peaks have previously been used to detect dislocation activity in nanocrystalline Ni

60 under uniaxial tension [11] and compression in a diamond anvil cell (DAC) [12]. These studies

61 involve the response at grain boundaries as well as within the grains, so they cannot be directly

62 applied to understand plasticity in individual nanocrystals. To do this, the structural response of

63 isolated nanocrystals must be obtained. This presents a challenge for *in situ* XRD because the

64 diffracted intensities from a single nanocrystal are much too small for detection.

65   Here, we use XRD to detect structural changes in an ensemble of monodisperse 3.9 nm

66 Au nanocrystals that are compressed under a non-hydrostatic pressure in a DAC. Surfaces of the

67 nanocrystals are protected by organic ligands, which prevents contact between the nanocrystals.

68 Structural changes from XRD are corroborated with optical spectroscopy measurements, and

69   MD simulations are used to determine the specific defects that correspond to the ensemble-

70   averaged behavior from XRD. We show that irreversible deformation due to the formation of

71   surface nucleated partial dislocations can occur in small metallic nanocrystals. This indicates that

72   dislocation-mediated plasticity is still active at single nanometer length scales and must be

73   considered in designing structures at this scale. In addition, a transition from collective to

74   localized dislocation nucleation events has been observed in theoretical studies of homogenous

75   dislocation nucleation [13,14], which can be compared to the DAC compression of extremely

76   small nanocrystals. These concepts have been tested using nanoindentation, but DAC

77   compression allows the examination of smaller samples under various stress states using in-situ

78   measurement techniques.

79   Au nanocrystals were synthesized using the organic phase reduction of chloroauric acid

80   and capped with dodecanethiol ligands [15]. The nanocrystal size distribution was found to be

81   3.9±0.6 nm using TEM (see Fig. 1A and see the Supplementary Material [16]). High-resolution

82   TEM images showed that most of the identified nanocrystals were either icosahedral or

83   decahedral in shape (Fig. 1B-C). Icosahedral nanocrystals have 20 twin boundaries, and

84   decahedral nanocrystals have 5 twin boundaries. Ambient pressure XRD showed an FCC crystal

85   structure, and significantly broader peaks than bulk Au due to the limited coherent scattering

86   volume within the nanocrystals (see the Supplementary Material [16]). The (111), (220), (311)

87   and (222) XRD peaks were shifted to higher 2θ angles by $\sim0.1^{\circ}$ compared to that of the bulk,

88   which corresponds to a $\sim1.8\%$ volumetric compressive strain. The position of the (200) peak was

89   shifted to lower 2θ angles by 0.15°. Broad shoulders were observed on the (200) and (220) peaks.

90   These features are indicative of the high twin density in icosahedral and decahedral

91   nanocrystals [24]. In addition, the (111) peak showed asymmetric broadening due to tensile and

92 compressive stresses at the surfaces and the interior of the nanocrystals due to surface

93 stresses [32]. The Au nanocrystals consist of ~20% surface atoms with most of the surface

94 covered with (111) planes. As a result, the (111) peak shows the most asymmetrical broadening

95 compared to the other peaks. The Debye scattering equation was used to fit the XRD pattern to

96 determine the structure of the nanocrystals. In this method, the atomic positions for icosahedral

97 and decahedral nanocrystals were generated for 1 to 6 nm diameter nanocrystals and used to

98 simulate XRD patterns. A Rietveld-like refinement procedure was used to fit the experimental

99 data [24,26]. The best fit was obtained by combining 60% icosahedral nanocrystals with a size

100 distribution of 3.2±0.2 nm and 40% decahedral nanocrystals with a size distribution of 3.8±0.6

101 nm (see the Supplementary Material [16]). This result is in close agreement with the nanocrystal

102 shape and size distribution observed in TEM.

103 High pressure XRD was obtained during DAC compression experiments at the Advanced

104 Light Source at Lawrence Berkeley National Laboratory (Fig. 2A-B). A non-hydrostatic pressure

105 was applied to the nanocrystals by loading the nanocrystals as a thick film at the bottom of the

106 DAC sample chamber, and using toluene as a non-hydrostatic pressure medium [33]. XRD was

107 collected while the nanocrystals were loaded up to 7.5 GPa and as pressure was released. The

108 pressure was limited to 7.5 GPa to avoid sintering between the nanocrystals, which has been

109 observed by our group and others at higher pressures [34–36]. The XRD peak position and

110 width (full width at half max) were observed to change with increasing and decreasing pressure

111 and quantified at each pressure (Fig. 2C-D). The relative intensity of the XRD peaks does not

112 change under pressure, which indicates that the nanocrystals remain randomly oriented.

113 The change in peak position indicates the elastic strain in the nanocrystals. The shift in

114 the peak position shows that the lattice spacing decreases by 0.042 Å over 7.5 GPa and recovers

115   to ~0.2% of its original value upon unloading. The (200) peak position gives information about

116   the extent of twinning in the sample (see Fig. S8 for the qualitative effect of twinning on the

117   XRD peak). The complete recovery of the (200) peak position indicates that the initial multiply

118   twinned structure (icosahedral/decahedral) is preserved after the pressure cycle. Due to the non-

119   hydrostatic pressure, the change in lattice spacing is different along the loading axis (axial) and

120   orthogonal to the loading axis (radial). The geometry of the X-ray setup is such that the

121   measured lattice spacings correspond to planes that are almost aligned with the loading axis.

122   Therefore, the measured change in lattice spacing is lower than in the hydrostatic case (see the

123   Supplementary Material [16]). The difference between radial and axial stress components

124   (termed as t) can give us an estimate of maximum deviatoric and shear stresses in the system.

125   This difference can be calculated by considering the elastic anisotropy of a polycrystalline, FCC

126   metal. We used lattice strain theory to get a rough estimate of 't' [31,37] (see the Supplementary

127   Material [16]). Using this we estimated the maximum shear stress of Au nanoparticles to be

128   about 2.3 GPa (see the Supplementary Material [16]).

129   Fig. 2D shows the change in peak width for the (111), (200) and (220) peaks with a

130   complete pressure cycle. The (200) peak width showed a significant increase of 16% and the

131   (220) peak width showed an increase of 23% with increasing pressure and remained at higher

132   values after unloading. This indicates that irreversible deformation is occurring in the

133   nanocrystals and remains in the nanocrystals on the time scale of the experimental

134   measurements. The XRD peak width can be affected by changes in crystallite size, shape and

135   microstrain [38]. It is possible that crystalline domains within the nanocrystal become elongated

136   under compression and split into smaller domains, but post-compression TEM images showed

137   that the nanocrystal shape and size distribution is identical to that of the as-synthesized

6

138 nanocrystals (see the Supplementary Material [16]). The (111) peak width is mostly affected by

139 domain size changes and is least affected by the presence of defects like twinning and stacking

140 faults in the nanocrystal (see the Supplementary Material [16]). The peak width for (111) peak

141 remained at about 2% of its initial value with pressure cycling. The insignificant change in the

142 (111) peak width also indicates that domain size does not change under pressure [24,39]. From

143 this analysis, we determine that the increased peak width after unloading is caused by the

144 formation of crystalline defects such as dislocations rather than changes in the size and shape of

145 crystalline domains. The observation that (200) and (220) peak were the most affected and the

146 (111) peak is least affected indicates the presence of stacking faults, twinning and dislocations

147 (see the Supplementary Material [16]).

148   These XRD results were corroborated by high-pressure optical absorbance spectroscopy.

149 Au nanocrystals have a plasmonic resonance that is dependent upon nanocrystal size, shape and

150 microstructure [40]. Previous optical modeling showed that the plasmon peak wavelength is

151 indicative of nanocrystal shape, while an irreversible decrease in the plasmon peak intensity is

152 indicative of the formation of crystalline defects [2]. The plasmon peak wavelength of the 3.9

153 nm Au nanocrystals increased by ~30 nm when pressure was increased to 7.5 GPa and recovered

154 its initial value upon unloading (see the Supplementary Material [16]). These optical

155 measurements showed that the nanocrystals elongate into ellipsoids and then recover their

156 original shape after unloading. The plasmon peak intensity showed an irreversible decrease after

157 unloading. The reduced absorbance peak intensity after unloading is correlated to the formation

158 of defects in nanocrystals through a damping factor [2]. The optical data supports the conclusion

159 that the irreversible increase in XRD peak width after pressure cycling is due to the formation of

160 crystalline defects, rather than a change in the size and shape of crystalline domains within the

7

161 nanocrystals. UV-vis absorbance provides conclusive information about nanocrystal shape, and

162 XRD provides conclusive information about defect formation.

163   MD simulations were used to understand the crystalline defects that form within the

164 nanocrystals, and their interactions with existing twin boundaries and surfaces. Two types of

165 stacking faults (SF) were formed in an icosahedral nanocrystal under pressure (Fig. 3A); SF type

166 1 refers to a stacking fault parallel to the outer surface of the nanocrystal (or parallel to surface

167 steps formed during deformation), and SF type 2 is a stacking fault parallel to an internal twin

168 boundary that intersects with two other twin boundaries. Both types of stacking fault were

169 formed by the nucleation and propagation of a Shockley partial dislocation with a Burgers vector

170 of $\frac{1}{6}\langle 112 \rangle a$. SF type 1 forms when a Shockley partial dislocation with Burgers vector parallel to

171 the outer surface propagates on a slip plane parallel to the outer surface. This results in a

172 displacement relative to adjacent grains that is about the magnitude of the Burgers vector (see the

173 Supplementary Material [16]). When trailing partials are activated on the same plane, the

174 stacking fault is removed, which results in the formation of a larger displacement. The trailing

175 partial slip in one grain sometimes triggers stacking fault formation in an adjacent grain. This

176 occurs if the Burgers vector of the trailing partial dislocation (i.e. the slip direction) is aligned

177 well with the Burgers vector of a leading partial dislocation (Fig. 3B). SF type 2 is a dislocation

178 that has a Burgers vector parallel to an interior twin boundary. The passage of SF type 2 is

179 blocked by intersecting twin boundaries and forms interfacial dislocations with a $\frac{1}{9}\langle 222 \rangle a$

180 Burgers vector. This type of stacking fault has also been observed in penta-twinned silver

181 nanowire with >40 nm diameter [41]. In contrast to the penta-twinned silver nanowires, the

182 trailing partial does not follow the leading partial (or, the SF type 2) in the 3.9 nm nanocrystal

183 because the image stress is very large due to the proximity to the free surface and opposes the

184 motion of the trailing partial. For this reason, SF type 2 is harder to form, and the plastic

185 deformation of the nanocrystal is dominated by the successive formation of SF type 1 defects.

186 This is in contrast with work by Sun et al. on Ag nanocrystals where they reported liquid like

187 deformation via surface diffusion; however, they had performed very high temperature MD

188 simulations to observe diffusion activity in MD time scale [1]. We conducted room-temperature

189 MD simulations where surface diffusion was limited. This is in line with experiments where the

190 Au nanocrystal surface was protected by bulky organic ligands that form Au-SR bonds which

191 prevent diffusion at the nanocrystal surface [42].

192   We attribute the irreversible deformation in the nanocrystals to SF type 1 defects, as

193 portions of these defects remain in the simulated nanocrystal after unloading (See Fig. 3B). The

194 stacking fault parallel to the outer surface is energetically meta-stable, because of the finite

195 energy barrier required to form a partial dislocation to reversely sweep out the stacking fault. In

196 experimental time scales, some meta-stable stacking faults can be expected to remain. In

197 contrast, SF type 2 escapes quickly to the free surface during unloading upon the removal of

198 deviatoric stress, which implies that the plastic deformation by this type of stacking fault is

199 reversible. SF type 2 forms a partial dislocation loop that is blocked by twin boundaries. This is

200 an unstable structure that is easily pulled towards the free surface by an image stress [41].

201   The correspondence between the experimental data and MD simulation was evaluated by

202 generating XRD patterns from the MD simulated structures at different pressures by using the

203 Debye scattering equation [26] (see Fig. 4A-B). The Debye scattering equation is a Fourier

204 transform of the interatomic distances in a nanocrystal. Large ripples are observed in the

205 computed patterns due to the small number of atoms in a finite sized nanocrystal (see Fig. S10).

206 These ripples become less prominent when diffraction patterns for different sized nanocrystals

207   are combined. Figure 4 shows the average XRD pattern for 3.5, 3.9, and 4.5 nm icosahedral and

208   4 nm decahedral nanocrystals to mimic the experimental nanocrystal size distribution. A small

209   ripple to the left of (111), and to the right of (200) and (220) can still be observed in Figure 4.

210   While these ripples could be further smoothened by simulating the same nanocrystal size

211   distribution as in experiments, this is infeasible due to constraints on computing time. The XRD

212   peaks were fitted using Lorentzian and Gaussian peak profile with a high order polynomial for

213   the background. Due to the ripple on the (220) peak, the exact (220) peak width cannot be

214   obtained but can still be analyzed qualitatively. The XRD peak width for the simulated patterns

215   showed a similar trend to experimental data in that the (111) peak width broadened the least, and

216   the (200) peak broadened the most under pressure (Fig. 4C-D). The (220) peak width also

217   increased, similarly to experiments (Fig. S11). The effect of adding stacking faults to the

218   nanocrystal is evident from the significant increase of peak width for the (200) and (220) peaks.

219   The close agreement of MD simulated XRD patterns and experimental XRD patterns shows that

220   MD simulations are a true representation of experiments.

221   In summary, using high-pressure XRD, optical absorbance spectroscopy and MD

222   simulations we provide the first evidence of plastic deformation in individual 3.9 nm Au

223   nanocrystals. The plastic deformation governed was by stacking faults formed via surface

224   nucleated partial dislocations. The formation of surface steps during the passage of sequential

225   partial dislocations as well as remaining stacking faults led to residual defects in the nanocrystal.

226   The kinetics of residual defect recovery after unloading the sample will be explored further in

227   future studies. This work provides a critical advancement in using experimental and simulation

228   generated XRD as a comprehensive measurement technique to study defect formation in

229   nanomaterials.

References

230

231   [1]   J. Sun, L. He, Y.-C. Lo, T. Xu, H. Bi, L. Sun, Z. Zhang, S. X. Mao, and J. Li, Nat. Mater.

232   **13**, 1007 (2014).

233   [2]   X. W. Gu, L. A. Hanson, C. N. Eisler, M. A. Koc, and A. P. Alivisatos, Phys. Rev. Lett.

234   **121**, 056102 (2018).

235   [3]   A. Sharma, N. Gazit, L. Klinger, and E. Rabkin, Adv. Funct. Mater. 1807554 (2019).

236   [4]   H. Zheng, A. Cao, C. R. Weinberger, J. Y. Huang, K. Du, J. Wang, Y. Ma, Y. Xia, and S.

237   X. Mao, Nat. Commun. **1**, 144 (2010).

238   [5]   P. Liu, L. Wang, Y. Yue, S. Song, X. Wang, K. M. Reddy, X. Liao, Z. Zhang, M. Chen,

239   and X. Han, Nanoscale **11**, 8727 (2019).

240   [6]   Y. Lu, J. Song, J. Y. Huang, and J. Lou, Nano Res. **4**, 1261 (2011).

241   [7]   J. Wei Wang, S. Narayanan, J. Yu Huang, Z. Zhang, T. Zhu, and S. X. Mao, Nat.

242   Commun. **4**, 2340 (2013).

243   [8]   L. Zhong, F. Sansoz, Y. He, C. Wang, Z. Zhang, and S. X. Mao, Nat. Mater. **16**, 439

244   (2017).

245   [9]   S. Sun, D. Kong, D. Li, X. Liao, D. Liu, S. Mao, Z. Zhang, L. Wang, and X. Han, ACS

246   Nano **13**, 8708 (2019).

247   [10]   D. Guo, G. Xie, and J. Luo, J. Phys. D. Appl. Phys. **47**, 013001 (2014).

248   [11]   Z. Budrovic, H. Van Swygenhoven, P. M. D. S. Van Petegem, and B. Schmitt, Science

249   **304**, 273 (2004).

250   [12]   B. Chen, K. Lutker, S. V. Raju, J. Yan, W. Kanitpanyacharoen, J. Lei, S. Yang, H. R.

251   Wenk, H. K. Mao, and Q. Williams, Science **338**, 1448 (2012).

252   [13]   R. Baggio, E. Arbib, P. Biscari, S. Conti, L. Truskinovsky, G. Zanzotto, and O. U.

253   Salman, Phys. Rev. Lett. **123**, 205501 (2019).

254   [14]   I. Plans, A. Carpio, and L. L. Bonilla, Epl **81**, 36001 (2008).

255   [15]   S. Peng, Y. Lee, C. Wang, H. Yin, S. Dai, and S. Sun, Nano Res. **1**, 229 (2008).

256   [16]   See Supplemental Material at [URL will be inserted by publisher], which includes Refs.

257   [2, 15, 17-31] for materials and methods, calculations, additional XRD and optical

258   absorbance spectroscopy.

259   [17]   C. Herbst, R. . Cook, and H. King, J. Non. Cryst. Solids **172–174**, 265 (1994).

260   [18]   H. K. Mao, J. Xu, and P. M. Bell, J. Geophys. Res. **91**, 4673 (1986).

261   [19]   C. Prescher and V. B. Prakapenka, High Press. Res. **35**, 223 (2015).

262   [20]   S. Plimpton, J. Comput. Phys. **117**, 1 (1995).

263   [21]   H. W. Sheng, M. J. Kramer, A. Cadien, T. Fujita, and M. W. Chen, Phys. Rev. B **83**,

264   134118 (2011).

265   [22]   W. G. Hoover and B. L. Holian, Phys. Lett. A **211**, 253 (1996).

266   [23]   A. Stukowski, Model. Simul. Mater. Sci. Eng. **18**, 015012 (2010).

267   [24]   A. Cervellino, C. Giannini, and A. Guagliardi, J. Appl. Crystallogr. **36**, 1148 (2003).

268   [25]   I. Kantor, V. Prakapenka, A. Kantor, P. Dera, A. Kurnosov, S. Sinogeikin, N.

269   Dubrovinskaia, and L. Dubrovinsky, Rev. Sci. Instrum. **83**, 125102 (2012).

270   [26]   A. Cervellino, R. Frison, F. Bertolotti, and A. Guagliardi, J. Appl. Crystallogr. **48**, 2026

271   (2015).

272   [27]   A. Dewaele, P. Loubeyre, and M. Mezouar, Phys. Rev. B **70**, 094112 (2004).

273   [28]   X. Hong, T. S. Duffy, L. Ehm, and D. J. Weidner, J. Phys. Condens. Matter **27**, 485303

274   (2015).

275   [29]   A. K. Singh, C. Balasingh, H. K. Mao, R. J. Hemley, and J. Shu, J. Appl. Phys. **83**, 7567

276 (1998).

277 [30] T. S. Duffy, G. Shen, D. L. Heinz, J. Shu, Y. Ma, H.-K. Mao, R. J. Hemley, and A. K.

278 Singh, Phys. Rev. B **60**, 15063 (1999).

279 [31] A. K. Singh, H. P. Liermann, S. K. Saxena, H. K. Mao, and S. U. Devi, J. Phys. Condens.

280 Matter **18**, S969 (2006).

281 [32] B. Palosz, E. Grzanka, S. Gierlotka, S. Stel´makh, R. Pielaszek, U. Bismayer, J.

282 Neuefeind, H.-P. Weber, T. Proffen, R. Von Dreele, and W. Palosz, Zeitschrift Für Krist. -

283 Cryst. Mater. **217**, 497 (2002).

284 [33] C. A. Herbst, R. L. Cook, and H. E. King Jr., J. Non. Cryst. Solids **172–174**, 265 (1994).

285 [34] B. Li, X. Wen, R. Li, Z. Wang, P. G. Clem, and H. Fan, Nat. Commun. **5**, 4179 (2014).

286 [35] B. Li, K. Bian, J. M. D. Lane, K. M. Salerno, G. S. Grest, T. Ao, R. Hickman, J. Wise, Z.

287 Wang, and H. Fan, Nat. Commun. **8**, 14778 (2017).

288 [36] Z. Wang, C. Schliehe, T. Wang, Y. Nagaoka, Y. C. Cao, W. A. Bassett, H. Wu, H. Fan,

289 and H. Weller, J. Am. Chem. Soc. **133**, 14484 (2011).

290 [37] A. K. Singh, J. Appl. Phys. **73**, 4278 (1993).

291 [38] B. D. Cullity and S. R. Stock, *Elements of X-Ray Diffraction* (2014).

292 [39] K. Takemura and A. Dewaele, Phys. Rev. B **78**, 104119 (2008).

293 [40] A. Vincenzo, P. Roberto, F. Marco, M. M. Onofrio, and I. Maria Antonia, J. Phys.

294 Condens. Matter **29**, 203002 (2017).

295 [41] R. A. Bernal, A. Aghaei, S. Lee, S. Ryu, K. Sohn, J. Huang, W. Cai, and H. Espinosa,

296 Nano Lett. **15**, 139 (2015).

297 [42] P. Ionita, A. Volkov, G. Jeschke, and V. Chechik, Anal. Chem. **80**, 95 (2008).
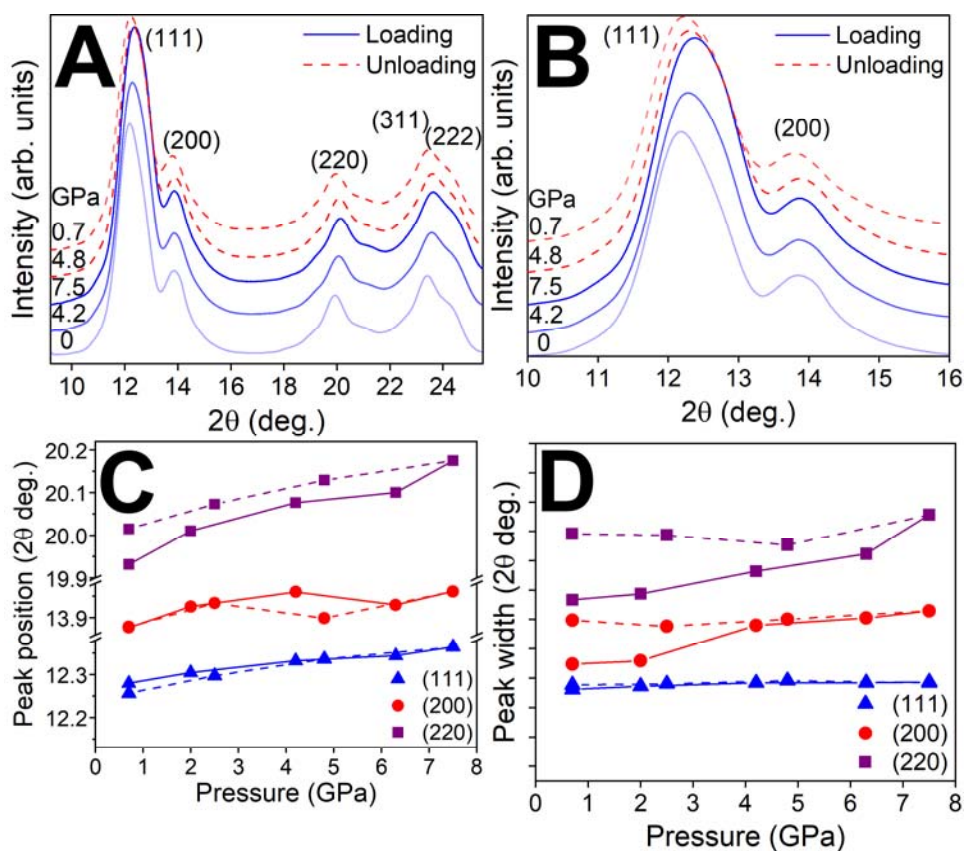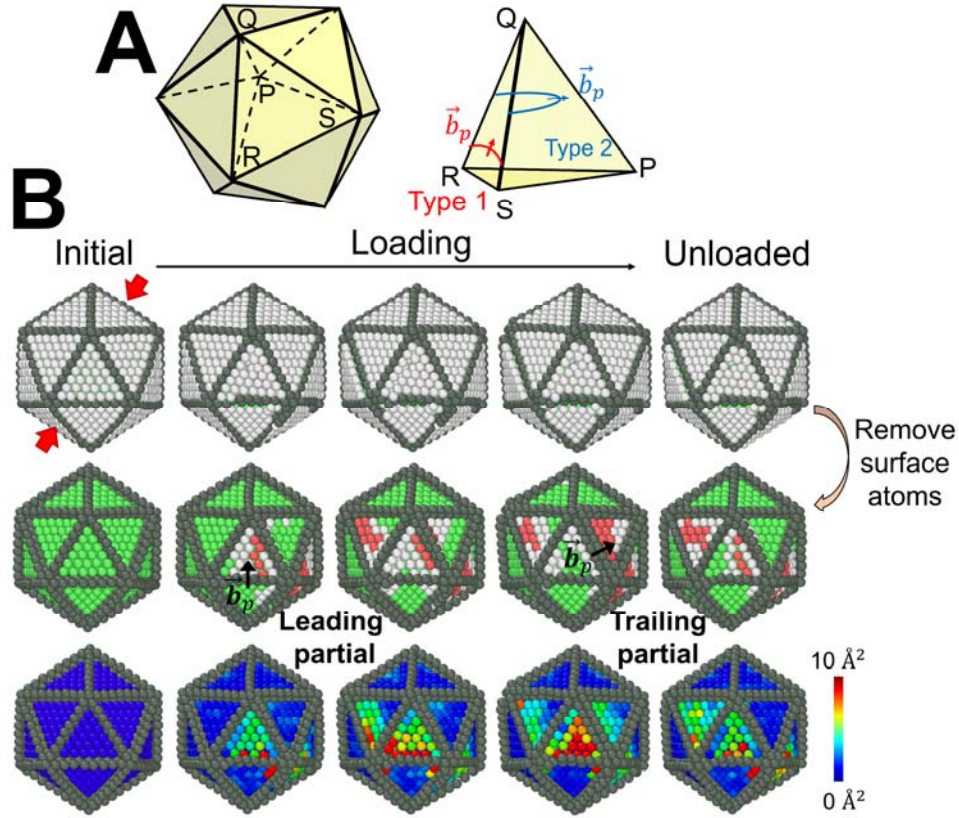
298

Figures

314

315 **Fig. 1. TEM images of nanocrystals.** A) Monodisperse 3.9 nm Au nanocrystals. Scale bar is 10

316 nm. High-resolution images of B) icosahedral and C) decahedral nanocrystals. Scale bar is 4 nm.
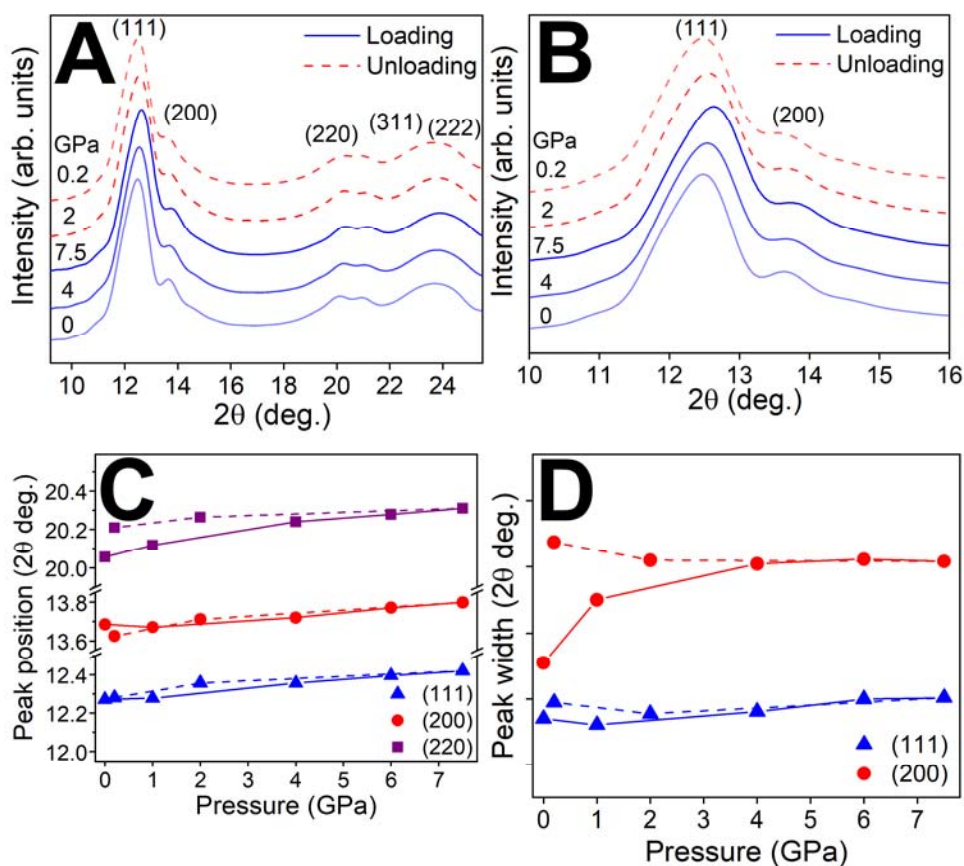
317

318

Fig. 2. Experimental high-pressure XRD patterns. A) All diffraction peaks and B) magnified

view of (111) and (200) peaks. Change in diffraction peak C) position and D) width (each

division is 0.1º), upon loading (solid line) and unloading (dashed line).

322

Fig. 3. MD simulation of a 3.9 nm icosahedral nanocrystal. A) Schematic of nanocrystal

geometry and slip planes for stacking fault type 1 and type 2. B) Atomic configurations during

loading and unloading process. Top row shows the surface atoms and the loading direction (red

arrows). In the next two rows, outermost atoms are omitted to visualize the formation of defects.

Images in middle row have green atoms for FCC, white atoms for unclassified crystal structure

(typically near the core of a partial dislocation or at the surface), and red atoms for HCP. Images

in bottom row are colored according to non-affine squared displacement, in which the slip plane

swept by a perfect dislocation is identified.

331

332

Fig. 4. Simulated high-pressure XRD patterns from MD simulations. A) All diffraction

peaks and B) magnified view of (111) and (200) peaks. Change in diffraction peak C) position

and D) width (each division is 0.1°), upon loading (solid line) and unloading (dashed line).

336